CHEMISTRY OF MATERIALS

pubs.acs.org/cm

Article

Kinetics and Evolution of Magnetism in Soft-Chemical Synthesis of $CrSe_2$ from $KCrSe_2$

Xiaoyu Song, Sarah N. Schneider, Guangming Cheng, Jason F. Khoury, Milena Jovanovic, Nan Yao, and Leslie M. Schoop*

Cite This: *Chem. Mater.* 2021, 33, 8070−8078

Read Online

ACCESS | Metrics & More | Article Recommendations | Supporting Information

ABSTRACT: Cation deintercalation with soft-chemical methods provides a route to synthesize new layered compounds with emergent physical and chemical properties that are inaccessible by conventional high-temperature solid-state synthesis methods. One example is $CrSe_2$, a van der Waals (vdW) material that is promising as an air-stable two-dimensional (2D) magnet. Cation deintercalation has rarely been studied mechanistically, and optimized reaction pathways to yield high-quality materials are often poorly understood. In this work, we perform a detailed study of the oxidative deintercalation process of $KCrSe_2$. We prove for the first time using high-resolution scanning transmission electron microscopy (STEM) that even though $CrSe_2$ indeed exists in a true vdW-layered structure, K-intercalated crystalline defects exist in the final product, even when an excess of oxidizing agent was used. We then study the kinetics of the oxidative deintercalation process, showing that it is a zeroth-order reaction with an activation energy of 0.27(6) eV, where the solid-state diffusion of K^+ cations in the potassium deintercalation process is the rate-limiting step. Finally, we study the relationship between Cr−Cr distances and the change in magnetic order by tracking how the properties change as a function of varying potassium content due to deintercalation. These data suggest that it might be possible to switch between magnetic states in $CrSe_2$ monolayers by varying its lattice parameters with methods, such as applying strain. Our study also provides a deeper understanding of the cation deintercalation process from a mechanistic perspective that will be helpful for the future development of synthetic methodology that can lead to other new layered materials.

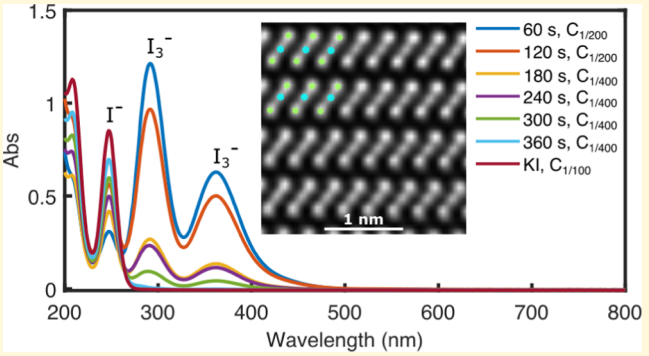

INTRODUCTION

Soft-chemical methods are an elegant way to synthesize new layered quantum materials with unconventional properties that typical high-temperature solid-state methods cannot directly access.[1−6] For example, $Na_xCoO_2{\cdot}1.3H_2O$ ($x \approx 0.3$), synthesized via the Br_2 oxidation of $Na_{0.7}CoO_2$, is a superconductor that displays a similar kind of chemical doping behavior as the high-temperature copper oxide superconductors.[7,8] 2M-WS_2, a metastable 1T′-type transition-metal dichalcogenide (TMD), synthesized by oxidizing $K_{0.7}WS_2$ with $K_2Cr_2O_7$ in aqueous H_2SO_4, has the highest reported superconducting transition temperature among TMDs and is predicted to be a topological superconductor.[9] Finally, van der Waals (vdW)-layered $CrSe_2$, a potential parent compound for air-stable ferromagnetic two-dimensional (2D) $CrSe_2$,[10] can be synthesized via K-deintercalation from $KCrSe_2$.[11] However, almost all of these reports focus on the properties of the product materials while overlooking the chemical process of deintercalation itself.

Generally, group VIB vdW-layered TMDs generate a lot of excitement as many members of this class can be easily exfoliated down to two dimensions and exhibit properties that their bulk forms do not have. For example, two-dimensional (2D) 1T-MoS_2 shows enhanced catalytic performance in the hydrogen evolution reaction.[12] 1T′-WTe_2 is the first known 2D topological insulator and is found to host a large variety of exotic physics, such as the quantum spin Hall effect, quantum oscillations in the insulating gap, or the presence of excitons in its ground state.[13−17] The lighter member of group VIB transition metals, Cr, could introduce intrinsic magnetism to TMDs, which would enrich their physical properties. However, vdW-layered bulk CrX_2 (X = S, Se, and Te) cannot be synthesized directly from the elements. van Bruggen et al. adapted the cation deintercalation method and synthesized metastable vdW-layered 1T-$CrSe_2$ from $KCrSe_2$ by I_2 oxidation in acetonitrile,[11] as shown in Figure 1. Bulk 1T-$CrSe_2$ adapts the

Received: July 29, 2021
Revised: September 21, 2021
Published: October 7, 2021

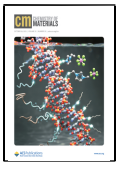

https://doi.org/10.1021/acs.chemmater.1c02620
Chem. Mater. 2021, 33, 8070−8078

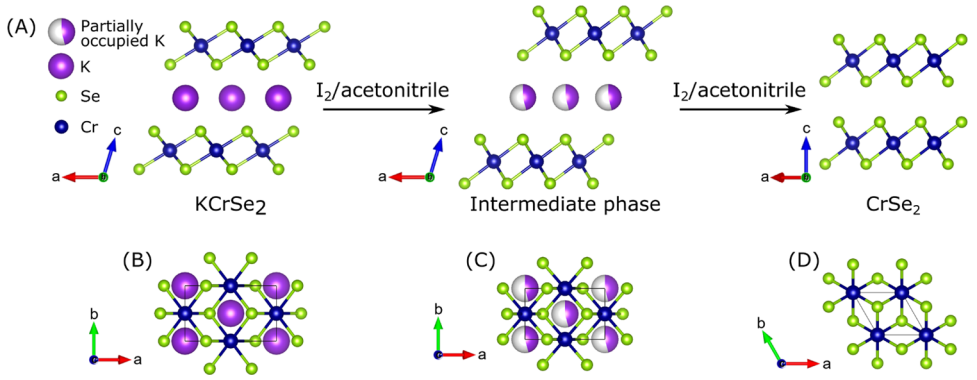

Figure 1. Illustration of the K-deintercalation process of $KCrSe_2$ by I_2 oxidation. The intermediate products are indicated by a partially occupied K^+.[25]

$Cd(OH)_2$-type structure and exhibits a charge density wave with linear Cr trimerization at low temperatures.[11,18] It has a metallic, antiferromagnetic ground state.[11,18,19] So far, 2D layers of $CrSe_2$ have not been exfoliated from the K-deintercalated bulk $CrSe_2$. Recently, however, $CrSe_2$ nanosheets were epitaxially grown on a WSe_2 substrate.[10] Unlike bulk $CrSe_2$, these epitaxially grown $CrSe_2$ nanosheets exhibit intrinsic ferromagnetism. In addition, they are robust in air, which is in contrast to most of the known magnetic nanosheets that tend to be highly air-sensitive, granting $CrSe_2$ potential for applications in magnetoelectronics and spintronics.[10] Therefore, it is clear that $CrSe_2$ is a promising 2D quantum material candidate, but there are many unresolved questions regarding its synthesis, stability, and magnetic properties. One point that should be clarified is whether bulk $CrSe_2$ is a true vdW material or if it suffers from defects as a result of Cr migration upon cation deintercalation. Such migration has been frequently observed in other layered Cr chalcogenides, such as $LiCrO_2$,[20] $NaCrO_2$,[21] $NaCrS_2$,[4,22,23] and $NaCr_{2/3}Ti_{1/3}S_2$.[24]

Currently, synthetic descriptions of $CrSe_2$ in the literature are rather vague and merely state that a "slight excess" of the stoichiometric ratio of I_2 was used for deintercalation.[11,18,26] To the best of our knowledge, the reaction has never been fully quantified and it seems unclear as to what types of impurities exist in the products. Although it has been shown that only very little K remains in samples, as no K-intercalated phase was detected in laboratory powder X-ray diffraction (PXRD), and chemical composition analysis revealed only traces of K,[11,18,26,27] the presence of any defects, even in very small fractions, can still have important ramifications for potential exfoliation. The impurity regions may hinder the 2D community to obtain uniform monolayers by mechanical exfoliation.[28] Despite several reports characterizing $CrSe_2$ via XRD, no direct atomic-resolution cross-sectional imaging has been reported on $CrSe_2$ so far. Such a cross-sectional analysis is critical, however, as it can reveal hidden defects (which, for example, could result from Cr migration or remaining K) in layered systems.[4]

In this work, we used XRD and high-resolution scanning transmission electron microscopy (STEM) to study the structural changes of $KCrSe_2$ during the K-deintercalation process. Then, we study the kinetics of K-deintercalation to understand this reaction from a chemical perspective. Previous kinetic studies on K-deintercalation in KNi_2Se_2 found that the process is likely zeroth-order,[29] but the reaction order had not been confirmed by time-dependent measurements. Here, we show that the deintercalation of $KCrSe_2$ is a zeroth-order reaction at room temperature with an Arrhenius activation energy of 0.27(6) eV. In addition, we investigate the magnetic properties of the intermediate, as well as end products, revealing a clear correlation of in-plane Cr−Cr distance and magnetic properties. A few previous works have studied the magnetism and lattice constant correlations in alkali metal-intercalated Cr dichalcogenides, usually comparing several different structural analogues.[30−33] In this study, we focus on one compound and study its magnetism and lattice constant correlations as we chemically modify its alkali cation content. $KCrSe_2$, which is used in this study as the starting compound, is known to exhibit A-type antiferromagnetism (AFM), where ferromagnetic (FM) layers are aligned antiparallel to each other.[34] However, when K is removed from the system, the magnetic order within the layers changes to AFM.[19] The cause of this has not yet been fully investigated. We believe that our study will help the community to gain a deeper understanding of the K-deintercalation reaction mechanism of $KCrSe_2$ and its magnetostructural correlations, along with further developing synthetic methodology for other vdW-layered compounds from alkali metal-intercalated compounds.

EXPERIMENTAL DETAILS

The synthesis of polycrystalline $KCrSe_2$ powder was based on previously published procedures.[11,34] The experiments of I_2 oxidation of $KCrSe_2$ powders were designed based on a previously published paper[11] and performed in an Ar-filled glovebox. Kinetic studies were based on both time and temperature. Details can be found in the Supporting Information (SI).

Powder X-ray diffraction (PXRD) patterns were collected on a STOE PXRD with Mo $K_{\alpha 1}$ radiation and a single-Mythen detector, working in the Debye−Scherrer geometry. Polycrystalline powders were ground with amorphous boron powders (PVZ nanoboron elemental amorphous boron powder with a >99 % boron content) in a 1:1 volume ratio in the Ar-filled glovebox before being sealed in 0.3 mm amorphous quartz capillaries for the measurements. The PXRD data were refined with the Fullprof Suite.[35] The crystallographic information framework (CIF) file from a previously published paper[18] was used for $CrSe_2$'s structural refinement.

Single-crystal X-ray diffraction (SCXRD) was performed on a small (∼100 μm) crystal picked from a powdered sample. Measurements were performed at 299(1) K on a Bruker APEX-II CCD diffractometer with Mo Kα radiation (λ = 0.71073 Å). A multiscan absorption correction was applied using SADABS. The data were solved using SHELXT with intrinsic phasing and refined with SHELXL via the least-squares method.[36]

For cross-sectional analysis, the samples were cut and transferred onto a Cu TEM grid with a Helios NanoLab G3 UC DualBeam FIB/SEM. The grid was then transferred to a Titan Cubed Themis 300 double Cs-corrected S/TEM. Details about sample preparation, transfer, microscopes, and image simulation can be found in the SI.

https://doi.org/10.1021/acs.chemmater.1c02620
Chem. Mater. 2021, 33, 8070−8078

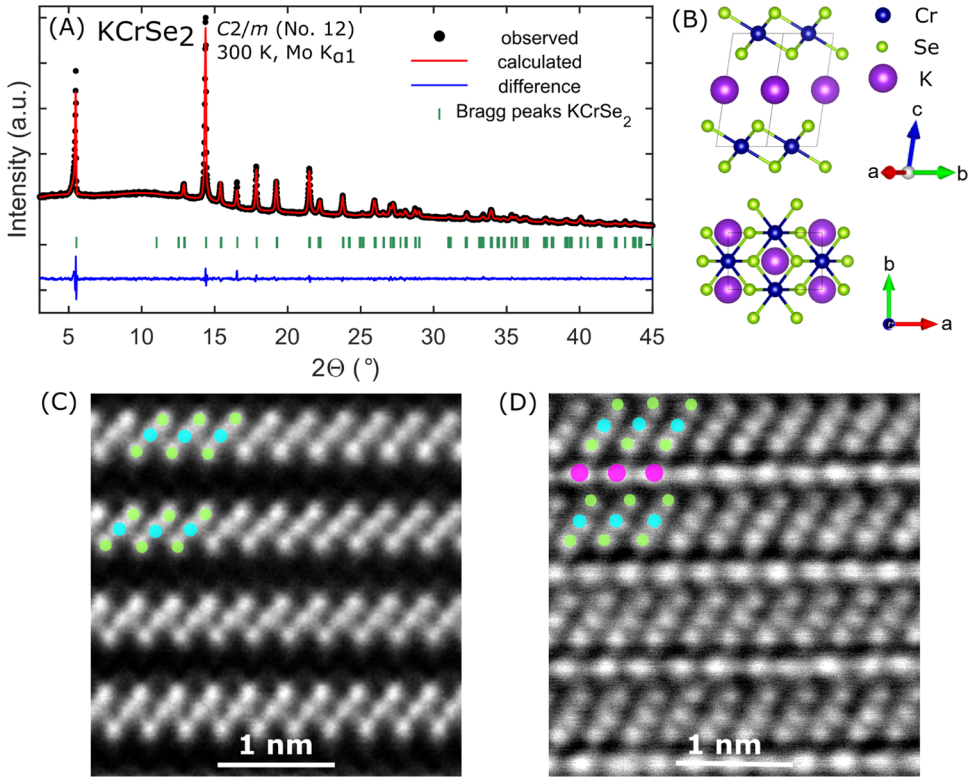

Figure 2. (A) Fitted powder XRD data of $KCrSe_2$ measured at room temperature with Mo $K_{\alpha 1}$ radiation; (B) crystal structure of $KCrSe_2$;[25] up: (110) plane, down: (001) plane; (C) a high-angular annual dark-field (HAADF) STEM image of $KCrSe_2$, zone axis [001] (green spheres represent Se atoms and cyan spheres represent Cr atoms); (D) an iDPC STEM image of $KCrSe_2$ at the same zone axis (green spheres represent Se atoms, cyan spheres represent Cr atoms, and magenta spheres represent K atoms).

The magnetic susceptibility data were acquired on a Quantum Design DynaCool Physical Property Measurement Setup (PPMS) with a vibrating sample magnetometer (VSM) model. Details about the scans can be found in the SI.

RESULTS AND DISCUSSION

Structure and Composition of $KCrSe_2$. Before studying the cation deintercalation process, we first carefully studied the parent compound $KCrSe_2$. Using SCXRD, we found that the $KCrSe_2$ has a different structure than previously published;[34,37,38] $KCrSe_2$ crystallizes in the monoclinic space group $C2/m$ (Table S1 gives the structural details). The structure found with SCXRD was then used for a Rietveld refinement of the PXRD pattern, which resulted in a good fit with an agreement factor (χ^2) of 2.15 and a Bragg factor (R_B) of 1.90. Figure 2A shows the fitted results, and structural parameters are listed in Table S2. In $KCrSe_2$, $[CrSe_2]^-$ slabs form a layered structure that is intercalated by K^+ cation layers, as shown in Figure 2B. Each Cr^{3+} atom is octahedrally coordinated by six Se^{2-} atoms, but unlike other sibling compounds, such as $LiCrSe_2$[33] and $NaCrSe_2$,[38] that crystallize in higher symmetry groups, the $CrSe_6$ octahedron is distorted with four longer Cr−Se bonds of length 2.58102(11) Å and two shorter Cr−Se bonds of length 2.55616(13) Å. Refinements of the PXRD pattern using the previously reported structure (space group $R\bar{3}m$)[34] result in poorer agreement factors due to lower calculated intensities for several peaks (i.e. the (0 0 9), (1 0 7), (0 1 8), (0 0 12), (1 0 10), (1 1 3), and (0 1 11) reflections). The intensities agree well if the space group $C2/m$ is used, which allows for the distorted $CrSe_6$ octahedra described above. This is in agreement with the solution found in SCXRD.

Previous reports suggested that the direct mixing of K, Cr, and Se is more likely to yield K-deficient phases, such as $K_{0.9}CrSe_2$[11,27] rather than the fully occupied $KCrSe_2$. However, both our SCXRD and PXRD refinement results indicate a full K occupancy in this compound but with a large displacement factor. This stoichiometric ratio is also confirmed by energy-dispersive spectroscopy (EDS), as shown in Figure S1 and Table S3. We noticed that some batches yield a mixture of $KCrSe_2$ and a K-deficient phase, most likely due to the volatility of K metal, but a single pure K-deficient phase was never isolated in our syntheses.

We then studied the cross-sectional structure of $KCrSe_2$ with high-resolution STEM to later compare with K-deintercalated samples. We noticed that high-angular annual dark-field (HAADF)-STEM images do not reveal any K^+ ions, as only $[CrSe_2]^-$ layers, separated by a large gap, are visible, as shown in Figure 2C. Such a large gap indicates that another layer of atoms should exist to stabilize the structure. STEM image simulations (Figure S2) of $KCrSe_2$ show that the K atoms have very weak contrast, which explains why they are not visible in real imaging conditions. To confirm the existence of K^+ layers, integrated differential phase contrast (iDPC) STEM[39] was performed on the same sample area, revealing the K^+ layers, as shown in Figure 2D.

Structural Evolution of $KCrSe_2$ during the I_2 Oxidation Process. Next, we investigated the structural evolution of $KCrSe_2$ during the K-deintercalation process. To obtain crystals with different degrees of K-deficiency, we added different volumes of 0.01 M I_2/acetonitrile solutions to the same amount of $KCrSe_2$ powders such that $KCrSe_2$ reacts with I_2 in molar ratios of 1:x (x = 0.05, 0.1, 0.2, 0.3, 0.45, 0.5, and 1.0) in each vial.

https://doi.org/10.1021/acs.chemmater.1c02620
Chem. Mater. 2021, 33, 8070−8078

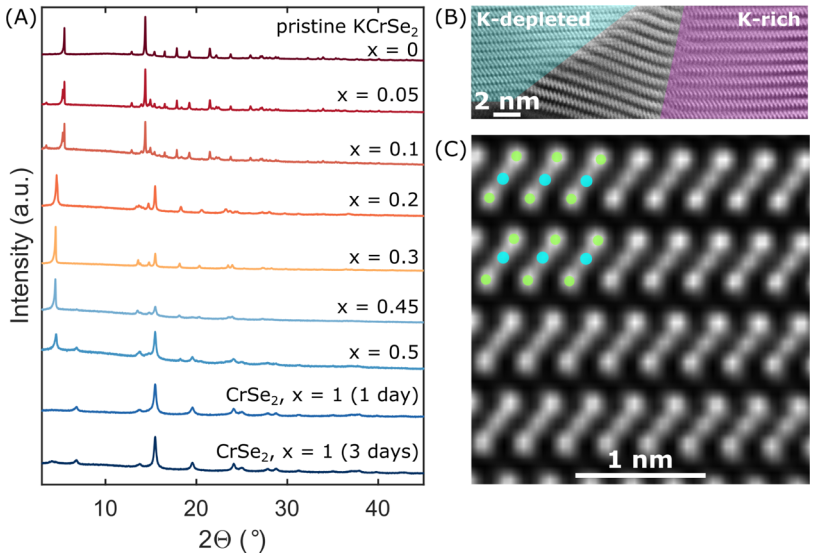

Figure 3. (A) PXRD of the products of $KCrSe_2$ reacts with I_2 in molar ratios of 1:x in comparison with $KCrSe_2$'s PXRD data (top) to show the trend of PXRD evolution during the K-deintercalation process; (B) a HAADF-STEM image showing the phase transition between the partially K-intercalated phase and $CrSe_2$, zone axis [001]; (C) an atomic-resolution image of $CrSe_2$, zone axis [001] (green spheres represent Se atoms and cyan spheres represent Cr atoms).

The normalized PXRD patterns of different reaction products together with the pristine $KCrSe_2$'s pattern are shown in Figure 3A to show the trend of the structural evolution. Refinements and structural parameters for each product are shown in SI (Figures S3−S10 and Tables S4−S11). In general, the substoichiometric reaction products consist of one to two K-deficient phases with the space group $C2/m$, the same as adopted by $KCrSe_2$. The stoichiometric $x = 0.5$ reaction product is a mixture of a K-deficient phase and $CrSe_2$, and the two overstoichiometric $x = 1$ reaction products both yielded $CrSe_2$ but with different lattice constants.

The products of the two lowest substoichiometric reactions ($x = 0.05$, 0.1) are similar and contain three phases. The majority phase is slightly K-deficient and has lattice parameters very close to those of pristine $KCrSe_2$. The second phase is more K-deficient, which leads to smaller in-plane lattice parameters, a larger c lattice constant, and a larger β angle. However, the layer distance, calculated by $c \times \sin \beta$, only experiences a slight change as compared to the pristine $KCrSe_2$ and the majority phase. The third phase is less than 5 wt % of the total product. This small impurity phase has a broadened (00l) peak at a low angle, almost half of $CrSe_2$'s (001) peak position. Thus, we tentatively assign this phase to a solvent-intercalated $CrSe_2$-type phase.

In the case of higher, but still substoichiometric I_2 amounts ($x = 0.2$, 0.3, 0.45), the products are more K-deficient but maintain the $C2/m$ space group. The resultant products have phases with larger interlayer distances and smaller intralayer Cr−Cr distances compared with the pristine $KCrSe_2$ and the main phases of the products of the two lowest substoichiometric reactions ($x = 0.05$, 0.1; see Tables S6−S8 for structural details). The product of reaction $x = 0.2$ is a mixture of two K-deficient phases, and the products of $x = 0.3$ and 0.45 are single phase. Thus, the optimized conditions to synthesize a pure, K-deficient phase with the structure shown in the middle panel of Figure 1 are $x = 0.3$ and 0.45. An abrupt increase of the layer distance and a decrease of in-plane lattice parameters are observed in the above phases as compared to $KCrSe_2$ and the phases in the products of the reactions with less I_2.

The product of the stoichiometric reaction ($x = 0.5$) is a mixture of monoclinic K-deficient $K_{0.7}CrSe_2$, based on the Rietveld analysis, and hexagonal vdW-layered $CrSe_2$. Note that the K content from the Rietveld analysis might not be very accurate in this case due to the multiphase analysis and fixed displacement factors. The lattice parameters of monoclinic K_yCrSe_2 are close to those found for the $x = 0.2$, 0.3, and 0.45 reactions. The hexagonal-layered $CrSe_2$ phase agrees well with the previously reported 1T-$CrSe_2$ structure.[18] The resultant mixture of a K-deficient phase and $CrSe_2$ at the stoichiometric reaction condition confirms that excess I_2 is important for a complete K-deintercalation reaction.[11] Therefore, we prepared an overstoichiometric reaction ($x = 1$) to see if twice the amount of I_2 is enough to remove all K. When the reaction was carried out for the same duration as the stoichiometric reaction ($x = 0.5$), the product's PXRD pattern can be fitted well with the 1T-$CrSe_2$ structure,[18] as shown in Figure S9. The broadened reflections in the PXRD pattern suggest the presence of defects in 1T-$CrSe_2$, which are likely caused by the oxidation process. We also kept the reaction running for a longer time ($x = 1$, 3 days) and found that the product of this reaction is also 1T-$CrSe_2$ (Figure S10), with slightly larger in-plane lattice parameters and a smaller layer distance (details in Tables S10 and S11). High-resolution STEM studies on the side view of 1T-$CrSe_2$ ($x = 1$, 3 days) reveal that small areas of K-intercalated $CrSe_2$ with larger layer distances, highlighted in purple in Figure 3B, coexist with the fully K-depleted $CrSe_2$ (marked by the blue color in the figure). This is in contrast with $NaCrS_2$, where Na^+ cations can be fully removed by proton exchange.[4] The gray region in the middle of Figure 3B connects the K-intercalated phase and K-depleted phase. An atomic-resolution image in the fully K-depleted region shows clean vdW $CrSe_2$ layers, as shown in Figure 3C. Our EDS analysis (Figure S11 and Table S12) confirms the presence of K in areas with larger layer distances and the absence of K in the K-depleted regions. In general, there are only very few regions that contain K; the majority of the sample is $CrSe_2$. A larger-scale image, where the amount of K is quantified, is shown in Figure S11. We also observed fewer K-rich regions in the 3 day sample as compared to those in the 1

https://doi.org/10.1021/acs.chemmater.1c02620
Chem. Mater. 2021, 33, 8070−8078

day sample. With our reaction conditions, we do not observe Cr migration to the interlayer space, which is common in other alkali-depleted $ACrX_2$ materials.[4,20−24] van Bruggen et al. had discussed that small amounts of native crystalline defects such as $K_{0.5}CrSe_2$ and Frenkel disorder defects from Cr migration likely exist in $CrSe_2$ made by the I_2 method, as these defects would explain their magnetic data.[11] They did not, however, provide direct proof of the existence of these disorder defects at the time. With our high-resolution STEM studies, we have confirmed the existence of K-intercalated crystalline defects but did not observe Frenkel disorder in $CrSe_2$ in our current experimental conditions. However, the appearance of Frenkel disorder could still be possible if harsher reaction conditions are applied.

Kinetics of the K-Deintercalation Process. The reaction order of the K-deintercalation process at room temperature was determined by the concentration of I^- (where $x = 0.1$), as a function of reaction times (60, 120, 180, 240, 300, and 360 s) (Figure S12 and Table S13). The fit of I^-'s concentration versus reaction time is linear (Figure 4A), while both the natural

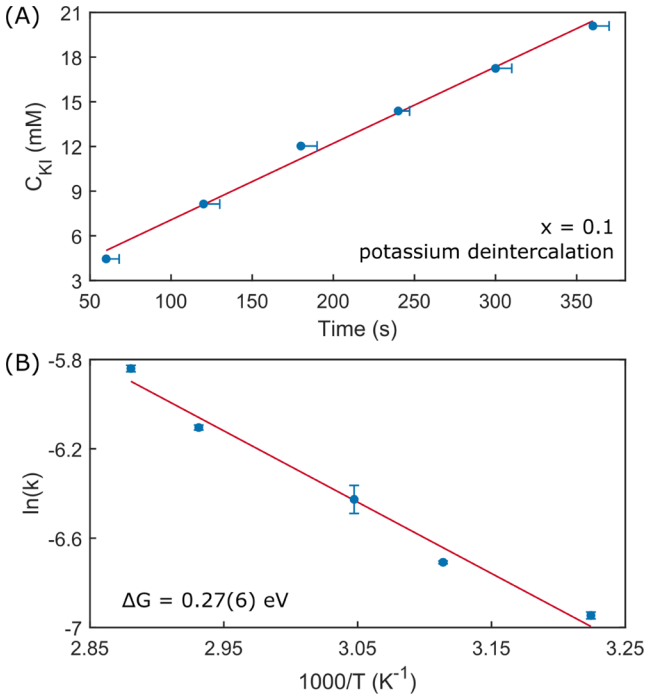

Figure 4. (A) Time dependence of I^- concentration [C_{I^-}] (blue). A linear fit of C_{I^-} versus reaction time shows that the K-deintercalation process is a zeroth-order reaction; (B) Arrhenius temperature dependence of the zeroth-order average rate constant (k) (blue) from 308 to 351 K, linearized as the natural logarithm [$\ln(k_{avg})$] as a function of the inverse reaction temperature [$1000/T$] (red) to estimate an activation barrier for the K-deintercalation process.

logarithm of I^- concentration versus reaction time and the inverse of I^- concentration versus reaction time gave nonlinear fits, as shown in Figure S13. Therefore, we determined that $KCrSe_2$'s K-deintercalation process is a zeroth-order reaction.

We subsequently studied the activation energy of the K-deintercalation reaction at the same $x = 0.1$ condition. The rates of K-deintercalation (k_{avg}) were determined by the end-of-reaction time at different temperatures (310.15, 321.15, 328.15, 341.15, and 347.15 K). For the reaction at $x = 0.1$, the activation energy was estimated from the Arrhenius relationship, $\ln(k_{avg}) = \Delta G/(RT) + \ln(k_0)$, where $\Delta G = 0.27(6)$ eV, as shown in Figure 4B. The experimentally determined activation energy for $x = 0.1$ in this study is similar to that of the early-stage K-deintercalation of KNi_2Se_2[29] and the diffusion of alkali metal ions in layered compounds,[40−42] validating that the rate of K-deintercalation limits the overall reaction rate, and solid-state diffusion of K^+ is the rate-limiting step for the overall reaction when $x \leq 0.1$.

Evolution of Magnetism upon Potassium Deintercalation. After having established the structural evolution during potassium deintercalation, it is of interest to investigate how this affects the magnetic properties. Pristine $KCrSe_2$'s A-type AFM behavior is evident in the $\chi-T$ plot (Figure 5A), which shows a decrease in susceptibility below the Néel temperature at 85 K, as well as a divergence of the ZFC and FC curves. A large positive Curie constant and prominent FM behavior in M−H data (Figure 5B) indicate strong FM interactions. The observed Néel temperature is different from that in an earlier report (40 K),[34] which can be attributed to the smaller applied magnetic field of 0.02 T in our measurement compared with the 0.861 T used in the earlier report. While measured with 0.861 T, the Néel temperature of our sample decreases to 53 K, suggesting that the decrease of Néel temperature with a higher applied field is intrinsic to $KCrSe_2$. The temperature-dependent inverse magnetic susceptibility of $KCrSe_2$ is almost linear in the high-temperature region. The Curie−Weiss fit of this region results in an effective magnetic moment of about 4.3 μ_B, higher than the theoretical magnetic moment for spin-only Cr^{3+} of 3.87 μ_B and the saturated moment extracted from the M−H data of 3.5(4) μ_B. An earlier study suggested that the nonlinearity in $1/\chi$ between 125 and 500 K is due to short-range order and that Curie−Weiss-type behavior is not reached until temperatures above 500 K, which is beyond our measurement range.[34] Therefore, we only show the linear fit line in the $1/\chi-T$ plot (Figure 5A) to highlight the positive Curie constant as an indication of strong FM intralayer interactions. The magnetization of $KCrSe_2$ increases linearly with the field (Figure 5B) until it saturates, indicating A-type AFM behavior, where the antiparallel aligned spins of the adjacent layers will align parallel as the magnetic field increases.

The first two substoichiometric reaction products ($x = 0.05$ and 0.1) also exhibit A-type AFM behavior and strong in-plane FM interactions (Figures S14 and S15). In the $\chi-T$ plots, both reaction products show a second Néel transition at around 120 K, besides the one around 85 K, which could come from the second K-deficient phase that is present in these products (Tables S4 and S5). In the M−H plots, a metamagnetic transition to the FM state (Figures S14B and S15B) at low field suggests that the interlayer coupling is weak.[18] The decrease of the saturation magnetic moment from 3.59 μ_B/Cr in $KCrSe_2$ to 2.59 μ_B/Cr when $x = 0.05$ and 2.53 μ_B/Cr when $x = 0.1$, respectively, indicates that the Cr^{3+} cations are oxidized as the K^+ cations deintercalate from the structure.

As more potassium cations are deintercalated from the layered system, the resultant reaction products ($x = 0.2$, 0.3, 0.45, 0.5, 1.0 for 1 day, and 1.0 for 3 days) show more prominent AFM behavior, as their field-dependent magnetization no longer saturates (Figures 5D, 6B, 6D, and S16B−S18B). The reaction product of the reaction with $x = 0.2$ is composed of two phases with similar crystal structures (Table S6), where the fraction of each phase is approximately 50 %. This can be seen in the broad Néel transition at around 79 K in the $\chi-T$ plot (Figure S16A). As the reaction product becomes single phase for $x = 0.3$, it exhibits a sharper transition at around 96 K. In the meanwhile, kinks start to appear in the high-temperature range from 150 to

https://doi.org/10.1021/acs.chemmater.1c02620
Chem. Mater. 2021, 33, 8070−8078

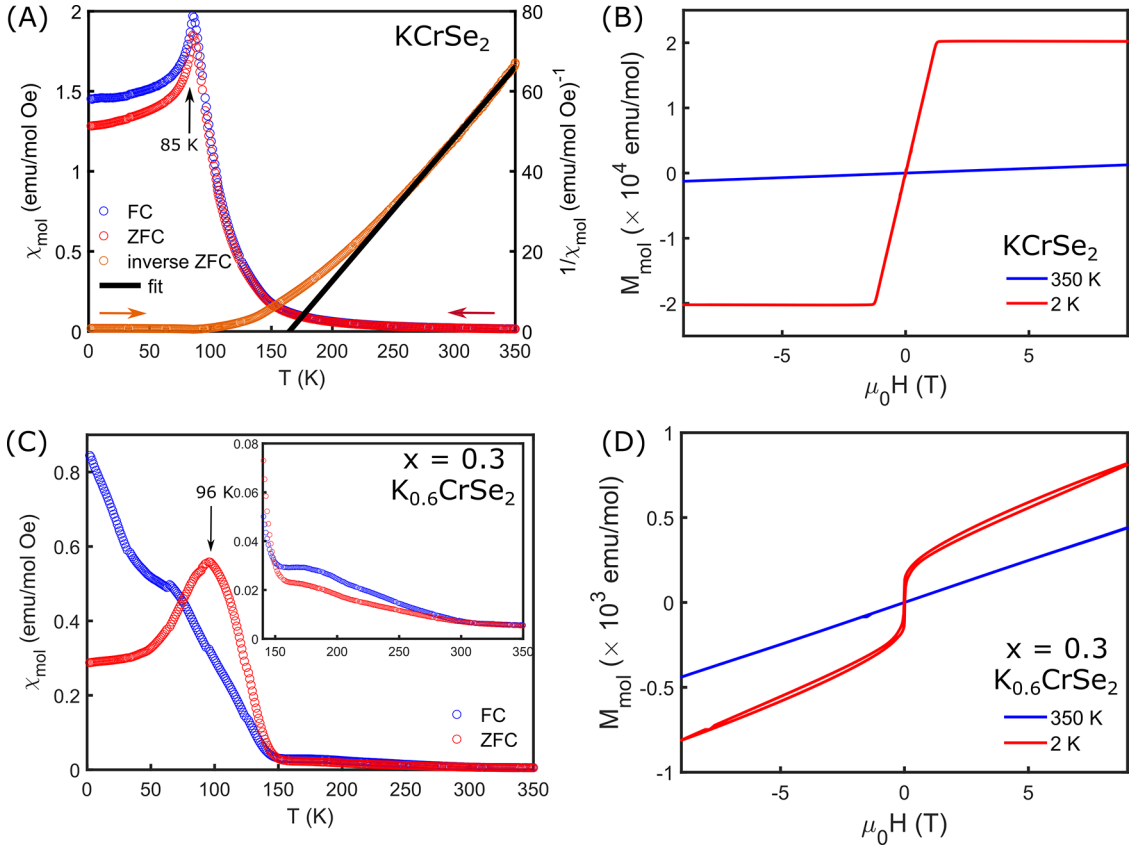

Figure 5. (A) Temperature-dependent magnetic susceptibility and inverse susceptibility of $KCrSe_2$; (B) field-dependent magnetization of $KCrSe_2$; (C) temperature-dependent magnetic susceptibility and inverse susceptibility of the reaction product for a reaction with a molar ratio of $KCrSe_2$:I_2 = 1:0.3; the insets highlight transitions at higher temperatures; and (D) field-dependent magnetization of the reaction product for a reaction with a molar ratio of $KCrSe_2$:I_2 = 1:0.3.

350 K and the $1/\chi-T$ curve is no longer linear, as shown in the inset of Figure 5C. This nonlinearity in $1/\chi$ might indicate short-range correlations. The high-temperature features are likely related to previously observed charge density wave (CDW) transitions in $CrSe_2$ around this temperature.[18] Interestingly, while the product of reaction with $x = 0.45$ shows a single phase in the PXRD (Figure S7 and Table S8), it shows multiple magnetic transitions between 40 and 130 K, as well as a prominent nonlinear behavior between 150 and 350 K in the $1/\chi-T$ plot (Figure S17A). The product of the stoichiometric reaction is a mixture of a K-intercalated phase and $CrSe_2$, which is reflected in its $1/\chi-T$ plot (Figure S18A), as one transition at around 85 K can be assigned to the AFM transition of the K-intercalated phase, while the other transition at around 25 K and multiple structural transitions at a temperature above 100 K are features of the $CrSe_2$ phase.[11,18,26,27]

The products of $x = 1.0$ (1 day) and $x = 1.0$ (3 days) are both phase-pure $CrSe_2$, as characterized by PXRD (Figures S9–S10 and Tables S10 and S11). However, small regions containing partially K-intercalated phase are seen under high-resolution STEM and EDS, as discussed earlier (Figures 3B and S11 and Table S12). This tiny amount of impurity is reflected in the low-temperature Curie tails seen in both samples' field-cooled χ–T curves (Figure 6A and C). Earlier papers on the magnetic properties of $CrSe_2$ synthesized with the same method also report the presence of a Curie tail, which was attributed to native defects of the remaining $K_{0.5}CrSe_2$, as well as Frenkel disorder defects resulting from Cr migration.[11,26,27] A clear paramagnetic to AFM transition can be seen around 35 K in both samples, which is close to that seen in the earlier report (42 K).[11] The nonsaturating increase of magnetization with an increasing field in the field-dependent magnetization plots also suggests that the majority phase is in the AFM state (Figure 6B,D). The small hysteresis loop in the M–H data indicates some canting of the spin or some disorder effects that result in a small net moment in the system, despite the overall AFM order. In the 1-day sample, successive structural changes can be seen in the $\chi-T$ plot from 76 to 260 K (Figure 6A). In the 3-day sample, a small cusp at 59 K corresponds to the Néel temperature of the K-intercalated phase (Figure 6C),[11] corresponding to the impurities that we observed in the STEM studies (Figures 3B and S11 and Table S12). Successive structural changes in the 3-day sample's $\chi-T$ plot merge into a broad transition that starts from 91 K and is seen until 250 K (Figure 6D). The susceptibility χ of the 3-day sample (Figure 6C) is an order of magnitude larger than that of the 1-day sample (Figure 6A), despite the fact that both samples are pure $CrSe_2$ under PXRD. Temperature-dependent magnetization measurements taken a year later on the same batch of a 3-day sample (which was stored in an Ar-filled glovebox) show the same magnetic transition in the $\chi-T$ plot as the freshly made 3-day sample, but χ increased further. PXRD on this sample shows extra peaks, suggesting that metastable $CrSe_2$ either decomposes or gradually transforms to a more stable phase over time. This is similar to K-deintercalated NiSe where a structural transformation of the metastable phase over time has been documented.[29] It is possible that the structural transformation or decomposition already occurs during the I_2 oxidation process when the reaction time is prolonged but is too small to be

https://doi.org/10.1021/acs.chemmater.1c02620
Chem. Mater. 2021, 33, 8070–8078

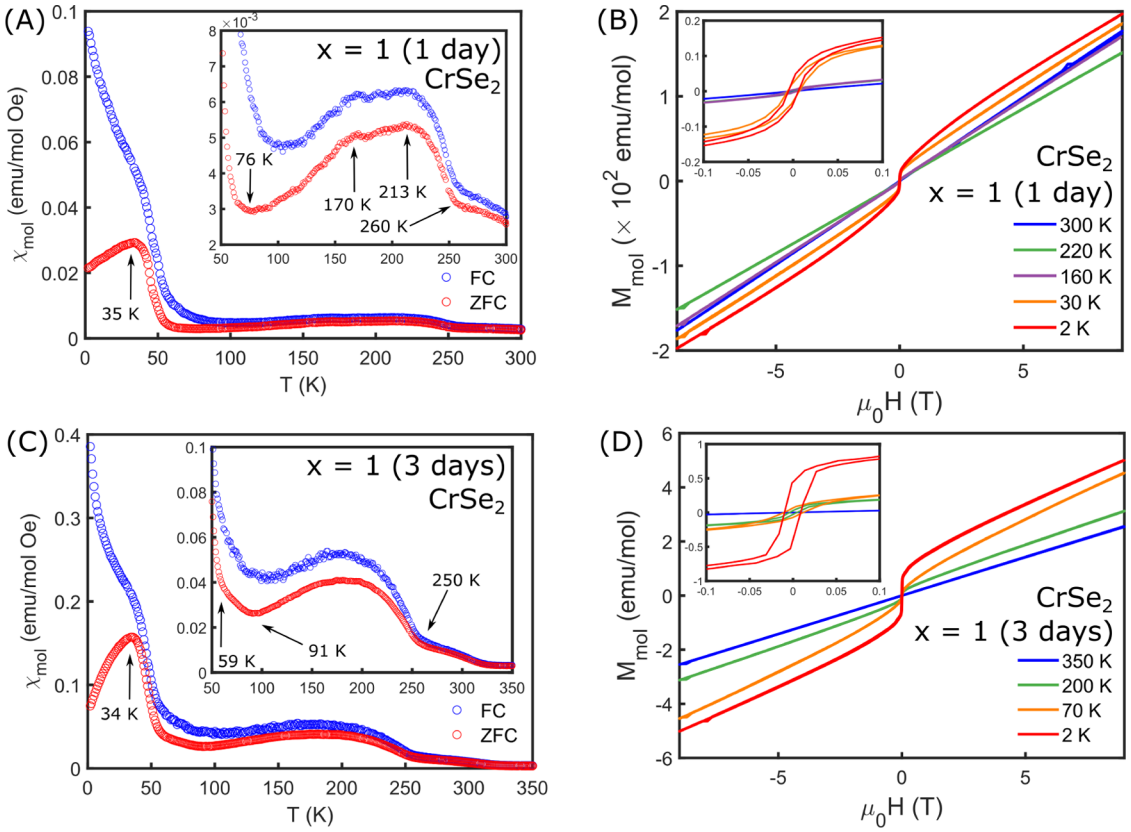

Figure 6. (A) Temperature-dependent magnetic susceptibility and inverse susceptibility of the reaction product for a 1-day reaction with a molar ratio of $KCrSe_2$:I_2 = 1:1; (B) field-dependent magnetization of the reaction product for a 1-day reaction with a molar ratio of $KCrSe_2$:I_2 = 1:1; (C) temperature-dependent magnetic susceptibility and inverse susceptibility of the reaction product for a 3-day reaction with a molar ratio of $KCrSe_2$:I_2 = 1:1; and (D) field-dependent magnetization of the reaction product for a 3-day reaction with a molar ratio of $KCrSe_2$:I_2 = 1:1.

captured by XRD or STEM at the time. The discrepancies in the two $CrSe_2$ samples show that the exact synthesis and defect control matter when investigating the properties of deintercalated materials.

Structure and Magnetic Correlations of the Reaction Products Obtained during the K-Deintercalation Process. Figure 7 puts the observed magnetic properties in correlation with the structural data discussed earlier. Note that here, the A-type AFM phase is labeled as FM, as this figure only refers to the intralayer magnetic order. If the $[CrSe_2]^-$ layers in this phase exist in monolayer form, the resulting sheets would be ferromagnets. Figure 7 highlights that the layer distance increases abruptly at the boundary between intralayer FM and AFM ordering, suggesting that the AFM interlayer superexchange interaction is weaker in the products of x = 0.2, 0.3, 0.45, and 0.5 compared with those in x = 0, 0.05, and 0.1. Therefore, we infer that intralayer AFM interactions are dominant in the products of x = 0.2, 0.3, 0.45, and 0.5 to result in an overall AFM behavior. This coincides with a drastic decrease of the closest intralayer Cr−Cr distance, as shown in Figure 7 at the same boundary. The overall in-plane magnetic behavior results from a competition of AFM direct exchange and the FM superexchange.[10,43] In the case of x = 0, 0.05, and 0.1, FM superexchange is more favored because of the larger Cr−Cr distance. In the case of x = 0.2, 0.3, 0.45, and 0.5, AFM direct exchange becomes dominant as the Cr−Cr distance decreases. In the fully oxidized products (x = 1.0, 1 day, and 3 days), the interlayer distance decreases by more than 2.5 Å, while the intralayer Cr−Cr distance also decreases further, leading to an AFM in-plane coupling and an overall AFM behavior.

The intralayer Cr−Cr distance plays a key role in the magnetic properties of $CrSe_2$, as a result of the competition between the AFM direct exchange and the FM superexchange within the layers.[10] In general, a larger Cr−Cr distance seems to favor FM over AFM; this was used to explain the FM behavior in epitaxially grown $CrSe_2$. Epitaxially grown 2D $CrSe_2$ has a lattice constant of 0.363 nm,[10] which falls into the FM section of our phase diagram, explaining the observed FM behavior in these nanosheets. We have demonstrated a way of fine-tuning $KCrSe_2$'s magnetism by K-deintercalation. Our results suggest that it might be possible to switch between magnetic states in $CrSe_2$ monolayers by varying its lattice parameters by, for example, applying external strain. Thus, $CrSe_2$ is a promising material for designing ultrathin magnetic switching devices.

CONCLUSIONS

In this work, we first performed a detailed structural characterization of $KCrSe_2$ and established its crystal structure in the monoclinic space group $C2/m$, which is different from the previously reported rhombohedral or hexagonal space groups. We subsequently partially and fully oxidized $KCrSe_2$ with different amounts of I_2 and studied the products' structural changes with PXRD and cross-sectional HRSTEM. Our HRSTEM analysis shows that small amounts of K-intercalated layered compounds coexist with fully deintercalated $CrSe_2$, even though PXRD might indicate phase-pure $CrSe_2$. These defects can contribute to the observed properties of $CrSe_2$, and

https://doi.org/10.1021/acs.chemmater.1c02620
Chem. Mater. 2021, 33, 8070−8078

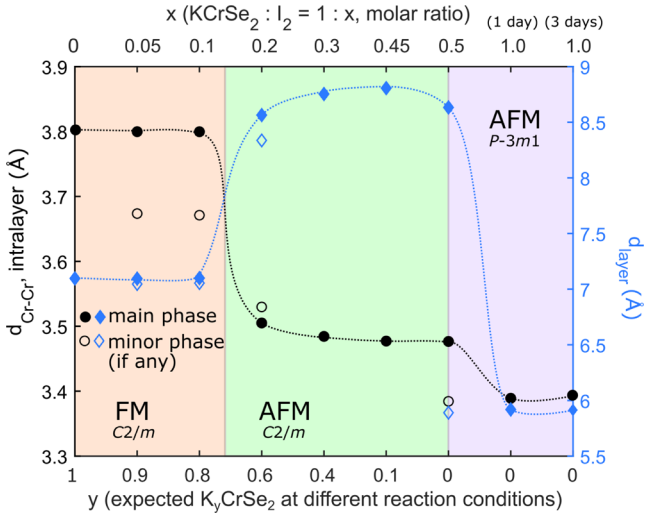

Figure 7. Phase diagram showing the structural and magnetic changes of reaction products obtained during the K-deintercalation process. The shortest intralayer Cr−Cr distance (black dots) and the interlayer distance (blue diamonds) of each reaction product are plotted against the expected K content in the product K_yCrSe_2 (lower x axis) at each reaction condition. The filled dots represent the data from the main phase of each product, and the unfilled dots and diamonds represent data from the minor phase of each product. The weight fractions for the main phases at x = 0.05, 0.1, 0.2, and 0.5 are 22.26, 24.50, 47.71, and 43.68%, respectively. The difference in intralayer magnetic interactions is differentiated by colored blocks, where orange represents ferromagnetic (FM) intralayer interactions, green represents antiferromagnetic (AFM) interactions in products with the $C2/m$ space group, and purple represents antiferromagnetic (AFM) interactions in products with the $P\bar{3}m1$ space group.

therefore, samples should be characterized carefully. Our kinetic study on the early-stage I_2 oxidation reaction of $KCrSe_2$ suggests that the overall oxidation reaction is zeroth-order, and K^+ solid-state diffusion is the rate-limiting step, with an activation barrier of 0.27(6) eV. Finally, we present the magnetic properties of the products obtained in the K-deintercalation process. Our results show that in the pristine $KCrSe_2$ and the products of early-stage oxidation, a relatively large intralayer Cr−Cr distance leads to dominant FM superexchange interactions within the plane, whereas with further oxidation, the products' in-plane lattices shrink and, therefore, result in an overall AFM coupling within the structure. Thus, the magnetic properties are closely related to structural details, which will be helpful for device design with the desired magnetic properties. We demonstrated a way of fine-tuning $KCrSe_2$'s magnetism by potassium cation deintercalation, as well as clarifying the synthetic and mechanistic conditions of the promising 2D magnetic material $CrSe_2$.

■ ASSOCIATED CONTENT

Supporting Information

The Supporting Information is available free of charge at https://pubs.acs.org/doi/10.1021/acs.chemmater.1c02620.

Crystallographic information framework ($KCrSe_2$) (CIF)
Detailed descriptions of all experimental procedures, SCXRD data, PXRD Rietveld refinement result, EDS, and simulated STEM image for $KCrSe_2$; PXRD data and Rietveld refinement results for the K-deintercalated products; STEM and EDS on $CrSe_2$; UV−vis spectra and kinetic studies of the K-deintercalation process; and additional magnetic susceptibility data (PDF)

■ AUTHOR INFORMATION

Corresponding Author

Leslie M. Schoop − *Department of Chemistry, Princeton University, Princeton, New Jersey 08544, United States;* orcid.org/0000-0003-3459-4241; Email: lschoop@princeton.edu

Authors

Xiaoyu Song − *Department of Chemistry, Princeton University, Princeton, New Jersey 08544, United States;* orcid.org/0000-0003-3384-0527

Sarah N. Schneider − *Department of Chemistry, Princeton University, Princeton, New Jersey 08544, United States*

Guangming Cheng − *Princeton Institute for Science and Technology of Materials, Princeton, New Jersey 08544, United States;* orcid.org/0000-0001-5852-1341

Jason F. Khoury − *Department of Chemistry, Princeton University, Princeton, New Jersey 08544, United States*

Milena Jovanovic − *Department of Chemistry, Princeton University, Princeton, New Jersey 08544, United States*

Nan Yao − *Princeton Institute for Science and Technology of Materials, Princeton, New Jersey 08544, United States*

Complete contact information is available at: https://pubs.acs.org/10.1021/acs.chemmater.1c02620

Notes

The authors declare no competing financial interest.

■ ACKNOWLEDGMENTS

This work was supported by the Gordon and Betty Moore Foundation through Grant GBMF9064 to L.M.S., the David and Lucile Packard Foundation, the Sloan Foundation, and the Princeton Catalysis Initiative (PCI). Additional support was provided by NSF through the Princeton Center for Complex Materials, a Materials Research Science and Engineering Center DMR-2011750. The authors acknowledge the use of Princeton's Imaging and Analysis Center, which is partially supported by the Princeton Center for Complex Materials, a National Science Foundation (NSF)-MRSEC program (DMR-2011750), and the use of the Department of Chemistry's core facility at Princeton University.

■ REFERENCES

(1) Song, X.; Yuan, F.; Schoop, L. M. The properties and prospects of chemically exfoliated nanosheets for quantum materials in two dimensions. *Appl. Phys. Rev.* **2021**, *8*, No. 011312.

(2) Uppuluri, R.; Gupta, A. S.; Rosas, A. S.; Mallouk, T. E. Soft chemistry of ion-exchangeable layered metal oxides. *Chem. Soc. Rev.* **2018**, *47*, 2401−2430.

(3) Chebiam, R.; Prado, F.; Manthiram, A. Soft Chemistry Synthesis and Characterization of Layered $Li_{1-x}Ni_{1-y}Co_yO_2$-δ ($0 \leq x \leq 1$ and $0 \leq y \leq 1$). *Chem. Mater.* **2001**, *13*, 2951−2957.

(4) Song, X.; Cheng, G.; Weber, D.; Pielnhofer, F.; Lei, S.; Klemenz, S.; Yeh, Y.-W.; Filsinger, K. A.; Arnold, C. B.; Yao, N.; Schoop, L. M. Soft Chemical Synthesis of H x CrS2: An Antiferromagnetic Material with Alternating Amorphous and Crystalline Layers. *J. Am. Chem. Soc.* **2019**, *141*, 15634−15640.

(5) Kim, T. W.; Ha, H.-W.; Paek, M.-J.; Hyun, S.-H.; Baek, I.-H.; Choy, J.-H.; Hwang, S.-J. Mesoporous iron oxide-layered titanate nanohybrids: Soft-chemical synthesis, characterization, and photocatalyst application. *J. Phys. Chem. C* **2008**, *112*, 14853−14862.

(6) Kobayashi, Y.; Tian, M.; Eguchi, M.; Mallouk, T. E. Ion-exchangeable, electronically conducting layered perovskite oxyfluorides. *J. Am. Chem. Soc.* **2009**, *131*, 9849−9855.

(7) Takada, K.; Sakurai, H.; Takayama-Muromachi, E.; Izumi, F.; Dilanian, R. A.; Sasaki, T. Superconductivity in two-dimensional CoO_2 layers. *Nature* **2003**, *422*, 53−55.
(8) Schaak, R. E.; Klimczuk, T.; Foo, M. L.; Cava, R. J. Superconductivity phase diagram of $Na_xCoO_2{\cdot}1.3H_2O$. *Nature* **2003**, *424*, 527−529.
(9) Fang, Y.; Pan, J.; Zhang, D.; Wang, D.; Hirose, H. T.; Terashima, T.; Uji, S.; Yuan, Y.; Li, W.; Tian, Z.; et al. Discovery of superconductivity in 2M WS_2 with possible topological surface states. *Adv. Mater.* **2019**, No. 1901942.
(10) Li, B.; et al. Van der Waals epitaxial growth of air-stable $CrSe_2$ nanosheets with thickness-tunable magnetic order. *Nat. Mater.* **2021**, *20*, 818−825.
(11) Van Bruggen, C.; Haange, R.; Wiegers, G.; De Boer, D. $CrSe_2$, a new layered dichalcogenide. *Phys. B+C* **1980**, *99*, 166−172.
(12) Lukowski, M. A.; Daniel, A. S.; Meng, F.; Forticaux, A.; Li, L.; Jin, S. Enhanced hydrogen evolution catalysis from chemically exfoliated metallic MoS_2 nanosheets. *J. Am. Chem. Soc.* **2013**, *135*, 10274−10277.
(13) Qian, X.; Liu, J.; Fu, L.; Li, J. Quantum spin Hall effect in two-dimensional transition metal dichalcogenides. *Science* **2014**, *346*, 1344−1347.
(14) Tang, S.; et al. Quantum spin Hall state in monolayer 1T′-WTe_2. *Nat. Phys.* **2017**, *13*, 683−687.
(15) Wu, S.; Fatemi, V.; Gibson, Q. D.; Watanabe, K.; Taniguchi, T.; Cava, R. J.; Jarillo-Herrero, P. Observation of the quantum spin Hall effect up to 100 kelvin in a monolayer crystal. *Science* **2018**, *359*, 76−79.
(16) Jia, Y.; Wang, P.; Chiu, C.-L.; Song, Z.; Yu, G.; Jäck, B.; Lei, S.; Klemenz, S.; Cevallos, F. A.; Onyszczak, M. et al. Evidence for a monolayer excitonic insulator. Submitted on 2020-10-12. arXiv.org (cond-mat). arXiv:2010.05390. (accessed 2021-09-21).
(17) Wang, P.; Yu, G.; Jia, Y.; Onyszczak, M.; Cevallos, F. A.; Lei, S.; Klemenz, S.; Watanabe, K.; Taniguchi, T.; Cava, R. J.; et al. Landau quantization and highly mobile fermions in an insulator. *Nature* **2021**, *589*, 225−229.
(18) Kobayashi, S.; Katayama, N.; Manjo, T.; Ueda, H.; Michioka, C.; Sugiyama, J.; Sassa, Y.; Forslund, O. K.; Månsson, M.; Yoshimura, K.; Sawa, H. Linear Trimer Formation with Antiferromagnetic Ordering in 1T-$CrSe_2$ Originating from Peierls-like Instabilities and Interlayer Se−Se Interactions. *Inorg. Chem.* **2019**, *58*, 14304−14315.
(19) Sugiyama, J.; Nozaki, H.; Umegaki, I.; Uyama, T.; Miwa, K.; Brewer, J. H.; Kobayashi, S.; Michioka, C.; Ueda, H.; Yoshimura, K. Static magnetic order on the metallic triangular lattice in $CrSe_2$ detected by μ SR+. *Phys. Rev. B: Condens. Matter Mater. Phys.* **2016**, *94*, No. 014408.
(20) Lyu, Y.; Ben, L.; Sun, Y.; Tang, D.; Xu, K.; Gu, L.; Xiao, R.; Li, H.; Chen, L.; Huang, X. Atomic insight into electrochemical inactivity of lithium chromate ($LiCrO_2$): Irreversible migration of chromium into lithium layers in surface regions. *J. Power Sources* **2015**, *273*, 1218−1225.
(21) Kubota, K.; Ikeuchi, I.; Nakayama, T.; Takei, C.; Yabuuchi, N.; Shiiba, H.; Nakayama, M.; Komaba, S. New insight into structural evolution in layered NaCrO2 during electrochemical sodium extraction. *J. Phys. Chem. C* **2015**, *119*, 166−175.
(22) Boller, H. Topotactic oxidation of $NaCrS_2$. *Solid State Ionics* **2001**, *141*−*142*, 53−56.
(23) Shadike, Z.; Zhou, Y.-N.; Chen, L.-L.; Wu, Q.; Yue, J.-L.; Zhang, N.; Yang, X.-Q.; Gu, L.; Liu, X.-S.; Shi, S.-Q.; Fu, Z.-W. Antisite occupation induced single anionic redox chemistry and structural stabilization of layered sodium chromium sulfide. *Nat. Commun.* **2017**, *8*, No. 566.
(24) Wang, T.; Ren, G.-X.; Shadike, Z.; Yue, J.-L.; Cao, M.-H.; Zhang, J.-N.; Chen, M.-W.; Yang, X.-Q.; Bak, S.-M.; Northrup, P.; Liu, P.; Liu, X.-S.; Fu, Z.-W. Anionic redox reaction in layered $NaCr_{2/3}Ti_{1/3}S_2$ through electron holes formation and dimerization of S-S. *Nat. Commun.* **2019**, *10*, No. 4458.
(25) Momma, K.; Izumi, F. VESTA 3 for three-dimensional visualization of crystal, volumetric and morphology data. *J. Appl. Crystallogr.* **2011**, *44*, 1272−1276.
(26) Freitas, D. C.; Nunez, M.; Strobel, P.; Sulpice, A.; Weht, R.; Aligia, A. A.; Nunez-Regueiro, M. Antiferromagnetism and ferromagnetism in layered 1 T-$CrSe_2$ with V and Ti replacements. *Phys. Rev. B: Condens. Matter Mater. Phys.* **2013**, *87*, No. 014420.
(27) Kobayashi, S.; Ueda, H.; Nishio-Hamane, D.; Michioka, C.; Yoshimura, K. Successive phase transitions driven by orbital ordering and electron transfer in quasi-two-dimensional $CrSe_2$ with a triangular lattice. *Phys. Rev. B: Condens. Matter Mater. Phys.* **2014**, *89*, No. 054413.
(28) Purbawati, A.; Coraux, J.; Vogel, J.; Hadj-Azzem, A.; Wu, N.; Bendiab, N.; Jegouso, D.; Renard, J.; Marty, L.; Bouchiat, V.; et al. In-plane magnetic domains and Néel-like domain walls in thin flakes of the room temperature CrTe2 van der Waals ferromagnet. *ACS Appl. Mater. Interfaces* **2020**, *12*, 30702−30710.
(29) Neilson, J. R.; McQueen, T. M. Bonding, ion mobility, and rate-limiting steps in deintercalation reactions with ThCr2Si2-type KNi2Se2. *J. Am. Chem. Soc.* **2012**, *134*, 7750−7757.
(30) Engelsman, F.; Wiegers, G.; Jellinek, F.; Van Laar, B. Crystal structures and magnetic structures of some metal (I) chromium (III) sulfides and selenides. *J. Solid State Chem.* **1973**, *6*, 574−582.
(31) Fang, C.; Van Bruggen, C.; De Groot, R.; Wiegers, G.; Haas, C. The electronic structure of the metastable layer compound. *J. Phys.: Condens. Matter* **1997**, *9*, 10173.
(32) Ushakov, A.; Kukusta, D.; Yaresko, A.; Khomskii, D. Magnetism of layered chromium sulfides $MCrS_2$ (M= Li, Na, K, Ag, and Au): A first-principles study. *Phys. Rev. B* **2013**, *87*, No. 014418.
(33) Kobayashi, S.; Ueda, H.; Michioka, C.; Yoshimura, K. Competition between the Direct Exchange Interaction and Super-exchange Interaction in Layered Compounds $LiCrSe_2$, $LiCrTe_2$, and $NaCrTe_2$ with a Triangular Lattice. *Inorg. Chem.* **2016**, *55*, 7407−7413.
(34) Fang, C. M.; Tolsma, P. R.; van Bruggen, C. F.; de Groot, R. A.; Wiegers, G. A.; Haas, C. Electronic structure and magnetic properties of $KCrSe_2$. *J. Phys.: Condens. Matter* **1996**, *8*, 4381−4388.
(35) Rodríguez-Carvajal, J. Recent advances in magnetic structure determination by neutron powder diffraction. *Phys. B* **1993**, *192*, 55−69.
(36) Sheldrick, G. M. *SHELXTL*, version 6.14; Bruker Analytical Xray Instruments, Inc.: Madison, WI, 2003.
(37) Dijkstra, J.; Van Bruggen, C.; Haas, C.; de Groot, R. Electronic structure of the half-metallic ferromagnet $KCrSe_2$. *Phys. Rev. B: Condens. Matter Mater. Phys.* **1989**, *40*, 7973.
(38) Rüdorff, W.; Ruston, W.; Scherhaufer, A. The crystal structure of sodium selenochromite, $NaCrSe_2$, and preliminary investigations on related compounds. *Acta Crystallogr.* **1948**, *1*, 196−200.
(39) Lazić, I.; Bosch, E. G.; Lazar, S. Phase contrast STEM for thin samples: Integrated differential phase contrast. *Ultramicroscopy* **2016**, *160*, 265−280.
(40) England, W.; Goodenough, J.; Wiseman, P. Ion-exchange reactions of mixed oxides. *J. Solid State Chem.* **1983**, *49*, 289−299.
(41) Van der Ven, A.; Thomas, J. C.; Xu, Q.; Swoboda, B.; Morgan, D. Nondilute diffusion from first principles: Li diffusion in LixTiS2. *Phys. Rev. B* **2008**, *78*, No. 104306.
(42) Kang, K.; Ceder, G. Factors that affect Li mobility in layered lithium transition metal oxides. *Phys. Rev. B* **2006**, *74*, No. 094105.
(43) Lv, H.; Lu, W.; Shao, D.; Liu, Y.; Sun, Y. Strain-controlled switch between ferromagnetism and antiferromagnetism in 1 T- CrX_2 (X= Se, Te) monolayers. *Phys. Rev. B: Condens. Matter Mater. Phys.* **2015**, *92*, No. 214419.

https://doi.org/10.1021/acs.chemmater.1c02620
Chem. Mater. 2021, 33, 8070−8078